



# LUND UNIVERSITY

## III-V Nanowire Complementary Metal-Oxide Semiconductor Transistors Monolithically Integrated on Si

Svensson, Johannes; Dey, Anil; Jacobsson, Daniel; Wernersson, Lars-Erik

*Published in:*  
Nano Letters

*DOI:*  
[10.1021/acs.nanolett.5b02936](https://doi.org/10.1021/acs.nanolett.5b02936)

2015

[Link to publication](#)

*Citation for published version (APA):*  
Svensson, J., Dey, A., Jacobsson, D., & Wernersson, L.-E. (2015). III-V Nanowire Complementary Metal-Oxide Semiconductor Transistors Monolithically Integrated on Si. *Nano Letters*, 15(12), 7898-7904.  
<https://doi.org/10.1021/acs.nanolett.5b02936>

*Total number of authors:*  
4

### General rights

Unless other specific re-use rights are stated the following general rights apply:  
Copyright and moral rights for the publications made accessible in the public portal are retained by the authors and/or other copyright owners and it is a condition of accessing publications that users recognise and abide by the legal requirements associated with these rights.

- Users may download and print one copy of any publication from the public portal for the purpose of private study or research.
- You may not further distribute the material or use it for any profit-making activity or commercial gain
- You may freely distribute the URL identifying the publication in the public portal

Read more about Creative commons licenses: <https://creativecommons.org/licenses/>

### Take down policy

If you believe that this document breaches copyright please contact us providing details, and we will remove access to the work immediately and investigate your claim.

LUND UNIVERSITY

PO Box 117  
221 00 Lund  
+46 46-222 00 00

# III–V Nanowire CMOS Monolithically Integrated on Si

Johannes Svensson<sup>\*1</sup>, Anil W. Dey<sup>\*1†</sup>, Daniel Jacobsson<sup>2</sup>, Lars-Erik Wernersson<sup>1</sup>

<sup>1</sup>Electrical and Information Technology, Lund University, Lund 221 00, Sweden

<sup>†</sup>Presently at Logic Technology Development, Intel Corporation, Hillsboro, Oregon, USA

<sup>2</sup>Solid State Physics/The Nanometer Structure Consortium, Lund University, Box 118, S-221 00 Lund, Sweden

<sup>\*</sup>These authors contributed equally

III–V semiconductors have attractive transport properties suitable for low-power, high-speed complementary metal-oxide-semiconductor (CMOS) implementation, but major challenges related to co-integration of III–V n- and p-type metal-oxide-semiconductor field-effect transistors (MOSFETs) on low-cost Si substrates have so far hindered their use for large scale logic circuits. Using a novel approach to grow both InAs and InAs/GaSb vertical nanowires of equal length simultaneously in one single growth step, we here demonstrate n- and p-type, III–V MOSFETs monolithically integrated on a Si substrate with high  $I_{on}/I_{off}$  ratios using a dual channel, single gate-stack design processed simultaneously for both types of transistors. In addition, we demonstrate fundamental CMOS logic gates, such as inverters and NAND gates, which illustrate the viability of our approach for large scale III–V MOSFET circuits on Si.

Keywords: III–V, CMOS, nanowire, inverter, NAND, InAs, GaSb, low-power logic, Si

Geometric scaling has for decades been the main technology drive for integrated Si circuits whereas materials integration plays an important role in the continued technology evolution. In future generations, III–V semiconductors are considered candidates to replace Si as channel material in MOSFETs due to their high mobilities and injection velocities that will enable voltage scaling to reduce the power consumption at maintained performance<sup>1</sup>. The recently demonstrated superior performance of III–V MOSFETs as compared to their Si counterparts<sup>2</sup> may be used for CMOS either in a single channel, e.g. InGaAs<sup>3</sup>, or a dual channel, e.g. InGaAs/Ge<sup>4, 5</sup> or InAs/GaSb<sup>6</sup> approach, with

benefits in simplicity for the single channel and performance for the dual channel approach. Previous efforts to integrate III–V materials on a Si platform have involved either transfer of channel material grown on a separate substrate<sup>4, 6–11</sup> or have exploited innovative growth techniques, such as aspect ratio trapping<sup>12</sup>, rapid melt growth<sup>3</sup>, lateral overgrowth<sup>13</sup> or template assisted growth<sup>14</sup>, to avoid high defect densities. Until now, a two-step transfer technique of molecular beam epitaxy (MBE) grown InGaSb and InAs layers used by Nah et al.<sup>8</sup> has been the only successful integration of both n- and p-type III-V materials into CMOS circuits on Si substrates. However, such methods are challenging to implement for large scale manufacturing due to the high cost of the initial wafers and the limited wafer size. In contrast, nanowire growth enables high III–V crystal quality on various substrates e.g. Si, as strain may relax radially<sup>15</sup> and wafer scale device fabrication has been demonstrated<sup>16</sup>. While there have been several reports on vertical III-V nanowire n-MOSFETs on Si<sup>17, 18</sup>, including demonstration of RF-circuits<sup>19</sup>, demonstrations of p-MOSFET integration have been lacking. Here we present fabrication of fundamental III–V CMOS digital circuits on Si in a vertical device layout comprising a gate-all-around nanowire transistor architecture, demonstrating a straightforward processing path for dual channel, single gate-stack, all III–V CMOS on Si.

The vertical device geometry is attractive, since it allows for aggressive gate length scaling due to the superior electrostatics of the gate-all-around geometry and a small device footprint enabling high density circuits. In addition, Yakimets et al. have predicted power savings of 10-15% for a vertical device layout as compared to a lateral geometry for the 7 nm technology node<sup>20</sup>. In this work we have focused on InAs and GaSb as the channel materials based on their respective high electron and hole mobilities suitable to achieve high performance of both n- and p-type MOSFETs<sup>1</sup> and demonstrate the growth of both materials on Si substrates by metal-organic vapor phase epitaxy (MOVPE) in a single growth step. The growth step reduces the need for complex processing simplifying fabrication saving cost and time. Both n- and p-type MOSFETs exhibit high  $I_{on}/I_{off}$  ratios using the same gate stack, which is known to be a critical concern for III–V MOSFETs.

51

52 n-InAs and p-GaSb nanowire segments were sequentially grown from electron beam lithography  
53 (EBL) patterned Au-particles of different sizes by the vapour-liquid-solid mechanism as displayed in  
54 Figure 1a-c. The substrate is high resistivity p-type Si with a 260 nm highly n-doped InAs layer that  
55 enables a low access resistance, straightforward device isolation, and high frequency operation<sup>21</sup>,  
56 which are substantial benefits as compared to growth approaches directly on Si<sup>17, 22</sup>. To achieve  
57 selective growth of both types of nanowires, we exploit the fact that the chemical potential of  
58 material dissolved in an Au particle during growth is increased with decreasing particle size due to  
59 the higher surface-to-volume ratio. Eventually, the chemical potential approaches that of the gas  
60 phase, reducing the driving force for material transport to the particles what is known as the Gibbs-  
61 Thompson effect<sup>23</sup>. Since the solubility for Sb in Au is small, the growth rate of GaSb is highly  
62 sensitive to the transport of Sb to the particle and thus for sufficiently small diameters, the growth  
63 can be completely suppressed. This size selective growth mechanism can be exploited for co-  
64 integration of InAs and InAs/GaSb nanowire arrays on the same Si substrate using a single growth run  
65 (Figure 1d) by first growing InAs and subsequently GaSb, and by precisely controlling the geometry  
66 and growth conditions as discussed in the following.

67 Scanning electron microscopy (SEM) inspection of nanowire arrays with different Au seed particle  
68 diameters ( $d_{Au}$ ) and pitches showed a diameter increase in the top segment of the nanowires for Au  
69 particles with  $d_{Au} > 30$  nm (Figure 2a). Transmission electron microscopy (TEM) with energy  
70 dispersive X-ray spectroscopy (XEDS) analysis (Supporting information figure S1) revealed that the  
71 diameter increase corresponds to the transition from InAs to GaSb. Such diameter increase has  
72 previously been attributed to the increased solubility of group III material in the Au particle in the  
73 presence of Sb<sup>24</sup>. For  $d_{Au} \leq 30$  nm, no diameter increase could be discerned in SEM (Figure 2a) and  
74 TEM analysis of wires from such arrays reveal that either no or only a very short GaSb segment has  
75 been grown. To study the dependence of Au diameter and pitch on the resulting nanowire

dimensions, the lengths and diameters of the InAs and GaSb segments were determined using the image analysis software NanoDim<sup>25</sup>. The length of the GaSb segments was found to increase with increasing  $d_{Au}$  while the length of the InAs segments exhibited the opposite trend (Figure 2c). The growth rate of InAs nanowires grown under similar conditions has been previously investigated and although there is a complex dependence on the exact array geometry and growth time, the rate was found to always decrease with Au diameter<sup>12</sup>. The observation of increased growth rate of GaSb for increasing  $d_{Au}$  is in accordance with what is predicted from the Gibbs-Thomson effect and corroborates previous results<sup>23</sup>. It can therefore be concluded that for  $d_{Au} \leq 30$  nm the growth of a GaSb segment is completely suppressed due to an insufficient supply of Sb for nucleation. This difference in growth rate between InAs and GaSb can be exploited to precisely control the nanowire length such that the InAs and InAs/GaSb nanowires reach the same final height which simplifies device processing. The possibility to select geometry and growth conditions to achieve similar lengths for the two types of nanowires simplifies the processing and device integration significantly since a common gate level can be used for both InAs and GaSb MOSFETs.

The length of the InAs segments was found increase with increasing nanowire pitch (Figure 2e). This effect can be attributed to the increasing competition for available precursor material collected from the substrate surface between the nanowires for decreasing pitch<sup>12</sup>. In contrast, the GaSb segments displayed no decrease in length down to 300 nm pitch, indicating that there is no competition for material collected from the substrate most likely due to the longer distance to the substrate and a shorter diffusion length of the precursors resulting in a smaller collection area. The diameters of both segments were found to be independent of the Au pitch (Figure 2d) demonstrating that the dependence of the InAs segment length on the pitch is not related to the nanowire diameter.

Transmission electron microscopy (TEM) was used to study InAs and InAs/GaSb nanowires grown from different  $d_{Au}$  (Figure 2h,i). The diffraction patterns from the InAs and the GaSb segments correspond to the wurtzite and zincblende crystal structures, respectively. Both segments are pure without any mixed crystal phases and the InAs segments have a stacking fault density of around  $30\ \mu\text{m}^{-1}$  and the GaSb segments have no stacking faults indicating a high crystal quality for both materials. XEDS analysis of the atomic constituents of the InAs segment revealed small amounts of Ga and Sb in a shell around the wire (supporting information figure S1). The thickness of this GaSb shell, which is formed during the growth of the GaSb segment, was calculated from the relative Ga content and the cross-section of the nanowire to be 1 nm.

Drive current matching between n- and p-type MOSFETs necessary for optimized circuit operation can be achieved by varying the number of nanowires in the two type of arrays. Thus far, we have demonstrated that the distance between InAs and InAs/GaSb nanowires can be as small as 200 nm (Figure 2f), which may enable a device packing density of n- and p-type MOSFETs difficult to obtain using other non-monolithic integration methods. The doping profile along the growth axis of the nanowires has been engineered to provide a non-intentionally doped channel and highly doped source/drain regions to reduce the access resistance. Sn was used as the n-type dopant for both the lower and upper part of the InAs segment, and Zn was used as the p-type dopant for the upper part of the GaSb segment (Figure 1c).

The broken band alignment of InAs and GaSb in combination with a high doping at the interface enables a high tunneling current, allowing the InAs segment to be used as an ohmic contact to the GaSb segment<sup>26</sup> where the gate is positioned in the p-MOSFETs. Vertical processing does not rely on high resolution lithography, but dimensions are instead defined by control of the deposition layer thicknesses or etch-back of deposited layers and thus allows for aggressive gate length scaling with accurate precision<sup>18</sup>. The subsequent device fabrication process includes atomic layer deposition of

the Al<sub>2</sub>O<sub>3</sub> gate dielectric and the formation of mesas, spacer layers, metal electrodes and interconnects by means of UV-lithography, wet etching, reactive ion etching and sputtering (Methods, Figure 2g and Supporting Information Figure S2)<sup>18, 27</sup>.

Individual transistors with 10 to 200 nanowires with a gate length of 200 nm have been processed simultaneously and electrically characterized. We obtain nanowire circumference normalized drive currents of  $I_{on} = 44 \mu\text{A}/\mu\text{m}$  and  $I_{on} = 7 \mu\text{A}/\mu\text{m}$  (Figure 3a) and transconductances of  $g_m = 95 \mu\text{S}/\mu\text{m}$  and  $g_m = 15 \mu\text{S}/\mu\text{m}$  at  $V_{ds} = 0.5 \text{ V}$  and a gate overdrive  $|V_{gs} - V_t| = 0.5 \text{ V}$ , for InAs and GaSb, respectively (Supporting Information Figure S3). The inverse subthreshold slope (SS) is 525 mV/decade and 300 mV/decade for InAs and GaSb, respectively. These relatively high values indicate that the gate action on the channel is not ideal and the electrostatics of these devices needs to be improved. To study the effect of the unintentional GaSb shell overgrown on the InAs segments, the GaSb shell was selectively removed by oxidation and wet etching in a different set of devices. This process is self-limiting and employed as a digital etching prior to the high- $\kappa$  deposition (Supporting Information Figure S4). In particular, for devices where the GaSb shell has been removed by digital etching, a SS of 180 mV/decade over two orders of magnitude for both InAs and GaSb is obtained at 0.5 V supply voltage (Figure 3b) indicating an improved gate control. The removal of the GaSb shell also gives an  $I_{on}/I_{off}$  ratio of  $10^3$  and  $10^4$  with a  $V_{GS}$  swing of 1 V for InAs and GaSb MOSFETs, respectively. These results demonstrate that a common gate stack may indeed be used for both transistor types in III-V CMOS. Even though these performance metrics are less impressive as compared to previous reports on individual In(Ga)As<sup>28</sup> and GaSb<sup>29</sup> MOSFETs it should be considered that there is only a limited number of previous reports on III-V CMOS integration on Si<sup>3, 6, 8, 30</sup>. The two step transfer technique reported by Nah et al. yielded  $I_{on} = 80 \mu\text{A}/\mu\text{m}$  and  $I_{on} = 22 \mu\text{A}/\mu\text{m}$  at 0.5 V gate overdrive and SS = 84 mV/dec and SS = 156 mV/dec for n-InAs and p-InGaSb devices, respectively<sup>8</sup>. Yokoyama et al. used a more straightforward single transfer technique of InAs/GaSb layers to Si resulting in ambipolar transfer characteristics with  $I_{on} = 4 \mu\text{A}/\mu\text{m}$  (at  $V_{ds} = 1 \text{ V}$ ,  $V_{gs} = 2 \text{ V}$ ) and  $I_{on} = 2.4 \mu\text{A}/\mu\text{m}$  (at  $V_{ds} = -1 \text{ V}$ ,  $V_{gs}$

= -4 V) for n- and p-type devices, respectively<sup>30</sup>. However, as discussed previously such transfer techniques are challenging to scale to larger wafers and the need for initial III-V substrates is costly. A more attractive route is to use monolithic integration techniques such as rapid melting growth<sup>3</sup> or lateral overgrowth<sup>13</sup>, however integration of both n- and p-type III-V transistors for CMOS circuits with channels directly grown on the same Si substrate has not previously been demonstrated. To improve the performance of our transistors,  $I_{on}$  and  $g_m$  have to be increased e.g. by the use of a self-aligned gate structure to avoid long ungated nanowire segments<sup>31</sup>. Further, to decrease the subthreshold slope the wire diameter should be reduced to improve electrostatics and the gate dielectric deposition optimized<sup>32</sup>.

In addition to individual MOSFETs, inverter circuits have also been fabricated as schematically depicted in Figure 4a. A supply voltage ( $V_{dd}$ ) between 0.25 and 1 V was applied to the top of the GaSb p-MOSFETs while the bottom of the InAs n-MOSFETs was connected to ground ( $V_{gnd}$ ). An input voltage ( $V_{in}$ ), applied to a gate electrode common for both transistors, was swept while the output voltage ( $V_{out}$ ) between the top of the InAs and the bottom of the GaSb nanowire arrays was measured. The voltage transfer characteristics of a typical inverter exhibit a maximum voltage gain of 2 V/V at  $V_{dd}=0.5$  V (Figure 4b). To study the transient response of the inverter, a 1 V square wave input signal is applied as  $V_{in}$ . The output signal follows the input signal up to 1 kHz (Figure 4c) but at higher frequencies it is distorted due to charging/discharging of the parasitic capacitances originating from the gate-to-drain and gate-to-source electrode overlaps. To increase the operating frequency, the gate and drain electrodes can be patterned using EBL, which has been shown to reduce parasitics considerably<sup>21</sup>. Furthermore, NAND gates with two InAs n-MOSFETs connected in series and two GaSb p-MOSFETs connected in parallel have also been implemented (Figure 4d,e). A supply voltage of  $V_{dd} = 1$  V is applied to the top of both of the GaSb p-MOSFETs while the bottom of one of the InAs n-MOSFETs is grounded and its top contact connected to the bottom of the other InAs n-MOSFET. Input voltages of  $V_{inA} / V_{inB} = \pm 1$  V used to for the four logic combinations '00', '01', '10' and '11' are



applied to two gate electrodes each connected to one pair of InAs / GaSb MOSFETs and the output voltage ( $V_{out}$ ) is measured between the n-InAs and the p-GaSb MOSFETs. The resulting output voltage is low only for  $V_{inA} = V_{inB} = 1$  V as expected. To improve the logic switching performance further, the drive currents of both types of MOSFETs should be increased by using larger nanowire arrays.

In conclusion, we have demonstrated a novel method enabling the monolithic co-integration of InAs and GaSb nanowires on Si substrates in one growth step. The lengths of the two materials can be independently controlled by the Au seed particle size and pitch which is crucial for vertical device and circuit fabrication using one gate level. That a single gate stack can be used for the fabrication of InAs n- and GaSb p-MOSFETs with high  $I_{on}/I_{off}$  ratios is also beneficial for simple device integration. The realization of both inverters and an NAND gates demonstrates that the fundamental building blocks necessary for more advanced digital logic circuits can be implemented using III-V channel materials directly grown on Si.

## METHODS

### Nanowire growth

Arrays of Au discs with a thickness of 15 nm and diameters from 22 nm to 42 nm were patterned by EBL on substrates consisting of 250 nm highly doped InAs layers grown on Si(111) substrates. The nanowires were grown using metalorganic vapor phase epitaxy (MOVPE) in an Aixtron 200/4 system at a pressure of 100 mbar and a total flow of 13000 sccm. After annealing at 550°C in arsine ( $AsH_3$ ), the InAs segment was grown at 420°C using trimethylindium (TMIn) and arsine with a molar fraction of  $X_{TMIn} = 2.79 \cdot 10^{-6}$  and  $X_{AsH_3} = 1.92 \cdot 10^{-4}$ , respectively. The bottom and top parts of the InAs segment were n-doped by triethyltin (TESn) with a molar fraction of  $X_{TESn} = 6.99 \cdot 10^{-7}$  and  $2.80 \cdot 10^{-6}$ , respectively, with an undoped segment inbetween. The sample was subsequently heated to 460°C in arsine, where the switch to GaSb growth was initiated while heating to 500°C for continued GaSb

growth with trimethylgallium (TMGa) and trimethylantimony (TMSb) with a molar fraction of  $X_{TMGa} = 5.79 \cdot 10^{-5}$  and  $X_{TMSb} = 1.04 \cdot 10^{-6}$ , respectively. In the top part of the GaSb segments diethylzinc ( $X_{DEZn} = 5.99 \cdot 10^{-6}$ ) is used for p-doping. The conditions for the GaSb growth have been optimized to suppress the growth of any GaSb segment for the smallest Au particles.

## TEM analysis

For crystal structure investigation, a JEOL 3000F TEM operating at 300kV with a point resolution of 1.7 Å was used. For high resolution TEM and selective area electron diffraction (SAED), the nanowires were imaged in the  $\langle -101 \rangle / \langle 11-20 \rangle$  zone axis. In addition, images were recorded using scanning TEM high angle annular dark field (STEM HAADF) for mass and thickness contrast. For chemical analysis, x-ray energy dispersive spectroscopy (XEDS) was used in both TEM and STEM mode. Nanowires were prepared for TEM analysis by mechanically breaking them off the growth substrate and transferred to copper grids covered with a lacey carbon layer.

## Device processing

All post-growth lithography is performed using photolithography. Atomic layer deposition (ALD) of 40 cycles of  $Al_2O_3$  at 250°C (EOT  $\approx$  1.7 nm) is used for the gate dielectric. The sample, for which the GaSb shell is removed, is oxidized for 10 min in ozone and etched 30 s in HF (1:100) just before ALD. Source mesa isolation is performed by etching the  $Al_2O_3$  in buffered oxide etch (1:10) for 20 s, and the InAs buffer layer in  $H_3PO_4:H_2O_2:H_2O$  (1:1:25) for 3 min. Photoresist (S1828) baked at 200°C for 1 h is employed as the separating spacers between the source and gate electrodes, as well as between the gate and drain electrodes. Thick resist is initially spin coated to achieve good planarization after which the thickness of the spacers is set by reactive ion etching (RIE) with oxygen. Following the first spacer, a 60 nm tungsten gate metal is sputtered and the gate length is set by a photoresist that is thinned down by RIE, followed by a dry-etch of tungsten in a  $SF_6/Ar$  plasma. After the second photoresist spacer, a Ti/W/Au top contact is sputtered. The top contact is patterned using photolithography and the three metals are etched using KI,  $H_2O_2$  and BOE (1:10).

227    **Electrical characterization**

228    DC characterization was carried out at room temperature using a Cascade 11000B probe station  
229    connected to a Keithley 4200 parameter analyzer.

230

231

- 233 1. del Alamo, J. A. *Nature* **2011**, 479, 317.
- 234 2. Sanghoon, L.; Cheng-Ying, H.; Cohen-Elias, D.; Thibeault, B. J.; Mitchell, W.;
- 235 Chobpattana, V.; Stemmer, S.; Gossard, A. C.; Rodwell, M. J. W. *IEEE Electron Device Lett.* **2014**, 35,
- 236 621.
- 237 3. Yuan, Z.; Kumar, A.; Chen, C.-Y.; Nainani, A.; Griffin, P.; Wang, A.; Wang, W.; Wong, M.
- 238 H.; Droopad, R.; Contreras-Guerrero, R.; Kirsch, P.; Jammy, R.; Plummer, J.; Saraswat, K. C.
- 239 *Symposium on VLSI Technology* **2013**, 54.
- 240 4. Czornomaz, L.; Daix, N.; Cheng, K.; Caimi, D.; Rossel, C.; Lister, K.; Sousa, M.;
- 241 Fompeyrine, J. *Electron Devices Meeting (IEDM)*, **2013**, 2.8.1.
- 242 5. Irisawa, T.; Oda, M.; Kamimuta, Y.; Moriyama, Y.; Ikeda, K.; Mieda, E.; Jevasuwan, W.;
- 243 Maeda, T.; Ichikawa, O.; Osada, T.; Hata, M.; Tezuka, T. *Symposium on VLSI Technology* **2013**, 56.
- 244 6. Dey, A. W.; Svensson, J.; Borg, B. M.; Ek, M.; Wernersson, L.-E. *Nano Lett.* **2012**, 12,
- 245 5593.
- 246 7. Ko, H.; Takei, K.; Kapadia, R.; Chuang, S.; Fang, H.; Leu, P. W.; Ganapathi, K.; Plis, E.;
- 247 Kim, H. S.; Chen, S.-Y.; Madsen, M.; Ford, A. C.; Chueh, Y.-L.; Krishna, S.; Salahuddin, S.; Javey, A.
- 248 *Nature* **2010**, 468, 286.
- 249 8. Nah, J.; Fang, H.; Wang, C.; Takei, K.; Lee, M. H.; Plis, E.; Krishna, S.; Javey, A. *Nano*
- 250 *Lett.* **2012**, 12, 3592.
- 251 9. Ahn, J.-H.; Kim, H.-S.; Lee, K. J.; Jeon, S.; Kang, S. J.; Sun, Y.; Nuzzo, R. G.; Rogers, J. A.
- 252 *Science* **2006**, 314, 1754.
- 253 10. Daix, N.; Uccelli, E.; Czornomaz, L.; Caimi, D.; Rossel, C.; Sousa, M.; Siegwart, H.;
- 254 Marchiori, C.; Hartmann, J. M.; Shiu, K.-T.; Cheng, C.-W.; Krishnan, M.; Lofaro, M.; Kobayashi, M.;
- 255 Sadana, D.; Fompeyrine, J. *APL Materials* **2014**, 2, 086104.
- 256 11. Nishi, K.; Yokoyama, M.; Yokoyama, H.; Hoshi, T.; Sugiyama, H.; Takenaka, M.; Takagi,
- 257 S. *Symposium on VLSI Technology*, **2015**, 174.
- 258 12. Waldron, N.; Merckling, C.; Teugels, L.; Ong, P.; Ibrahim, S. A. U.; Sebaai, F.;
- 259 Pourghaderi, A.; Barla, K.; Collaert, N.; Thean, A. V. Y. *IEEE Electron Device Lett.* **2014**, 35, 1097.
- 260 13. Czornomaz, L.; Uccelli, E.; Sousa, M.; Deshpande, V.; Djara, V.; Caimi, D.; Rossell, M. D.;
- 261 Erni, R.; Fompeyrine, J. *Symposium on VLSI Technology*, **2015**, 172.
- 262 14. Schmid, H.; Borg, M.; Moselund, K.; Gignac, L.; Breslin, C. M.; Bruley, J.; Cutaia, D.; Riel,
- 263 H. *Appl. Phys. Lett.* **2015**, 106, 233101.
- 264 15. Favre-Nicolin, V.; Mastropietro, F.; Eymery, J.; Camacho, D.; Niquet, Y. M.; Borg, B. M.;
- 265 Messing, M. E.; Wernersson, L. E.; Algra, R. E.; Bakkers, E. P. A. M.; Metzger, T. H.; Harder, R.;
- 266 Robinson, I. K. *New Jour. Phys.* **2010**, 12, 035013.
- 267 16. Ghalamestani, S. G.; Johansson, S.; Borg, B. M.; Lind, E.; Dick, K. A.; Wernersson, L. E.
- 268 *Nanotechnology* **2012**, 23, 015302.
- 269 17. Tomioka, K.; Yoshimura, M.; Fukui, T. *Nature* **2012**, 488, 189.
- 270 18. Persson, K. M.; Berg, M.; Borg, M. B.; Jun, W.; Johansson, S.; Svensson, J.; Jansson, K.;
- 271 Lind, E.; Wernersson, L. E. *IEEE Trans. Electron Devices* **2013**, 60, 2761.
- 272 19. Persson, K. M.; Berg, M.; Sjöland, H.; Lind, E.; Wernersson, L. E. *Electron. Lett.* **2014**,
- 273 50, 682.
- 274 20. Yakimets, D.; Eneman, G.; Schuddinck, P.; Trong Huynh, B.; Bardon, M. G.; Raghavan,
- 275 P.; Veloso, A.; Collaert, N.; Mercha, A.; Verkest, D.; Voon-Yew Thean, A.; De Meyer, K. *IEEE Trans.*
- 276 *Electron Devices* **2015**, 62, 1433.
- 277 21. Johansson, S.; Memisevic, E.; Wernersson, L. E.; Lind, E. *IEEE Electron Device Lett.*
- 278 **2014**, 35, 518.
- 279 22. Rehnstedt, C.; Martensson, T.; Thelander, C.; Samuelson, L.; Wernersson, L. E. *IEEE*
- 280 *Trans. Electron Devices* **2008**, 55, 3037.
- 281 23. Ek, M.; Borg, B. M.; Johansson, J.; Dick, K. A. *ACS Nano* **2013**, 7, 3668.

24. Jeppsson, M.; Dick, K. A.; Wagner, J. B.; Caroff, P.; Deppert, K.; Samuelson, L.; Wernersson, L.-E. *Jour. Cryst. Growth*. **2008**, *310*, 4115.
25. NanoDim Software, <http://www.nanodim.net>.
26. Takei, K.; Madsen, M.; Fang, H.; Kapadia, R.; Chuang, S.; Kim, H. S.; Liu, C.-H.; Plis, E.; Nah, J.; Krishna, S.; Chueh, Y.-L.; Guo, J.; Javey, A. *Nano Lett.* **2012**, *12*, 2060.
27. Thelander, C.; Froberg, L. E.; Rehnstedt, C.; Samuelson, L.; Wernersson, L. E. *IEEE Electron Device Lett.* **2008**, *29*, 206.
28. Lee, S.; Chobpattana, V.; Huang, C. Y.; Thibeault, B. J.; Mitchell, W.; Stemmer, S.; Gossard, A. C.; Rodwell, M. J. W. *Symposium on VLSI Technology*, **2014**, 1.
29. Chu, R. L.; Chiang, T. H.; Hsueh, W. J.; Chen, K. H.; Lin, K. Y.; Brown, G. J.; Chyi, J. I.; Kwo, J.; Hong, M. *Appl. Phys. Lett.* **2014**, *105*, 182106.
30. Yokoyama, M.; Yokoyama, H.; Takenaka, M.; Takagi, S. *Symposium on VLSI Technology*, **2014**, 1.
31. Berg, M.; Persson, K. M.; Kilpi, O. P.; Svensson, J.; Lind, E.; Wernersson, L. E. *Electron Devices Meeting (IEDM)*, **2015**.
32. Fu, C. H.; Lin, Y. H.; Lee, W. C.; Lin, T. D.; Chu, R. L.; Chu, L. K.; Chang, P.; Chen, M. H.; Hsueh, W. J.; Chen, S. H.; Brown, G. J.; Chyi, J. I.; Kwo, J.; Hong, M. *Microelectronic Engineering* **2015**, *147*, 330.

Supporting Information. Compositional analysis by XEDS line scans of InAs-GaSb nanowires. SEM images of various stages in an inverter fabrication process. Linear transfer characteristics and transconductance of InAs and GaSb MOSFETs. SEM images of a InAs-GaSb nanowire before and after digital etching.

## Acknowledgements

The authors would like to Erik Lind at the Department of Electrical and Information Technology, Lund University, for assistance. This work has been supported by the Swedish Research Council, the Swedish Foundation for Strategic Research, and the European Union 7th Framework Program E2SWITCH (Grant Agreement No. 619509).

## Author Contributions

J.S. grew the nanowires. A.D. and J.S. fabricated the devices and circuits and did DC characterization and data analysis. D.J. performed TEM imaging and analysis. The project was directed and supervised by L-E.W. A.D. and J.S. wrote the manuscript with considerable input from L-E.W. All authors discussed the data and commented on the manuscript.

## Competing financial interests

The authors declare no competing financial interests. Readers are welcome to comment on the online version of the paper. Correspondence and requests for materials should be addressed to L-E.W. (lars-erik.wernersson@eit.lth.se).

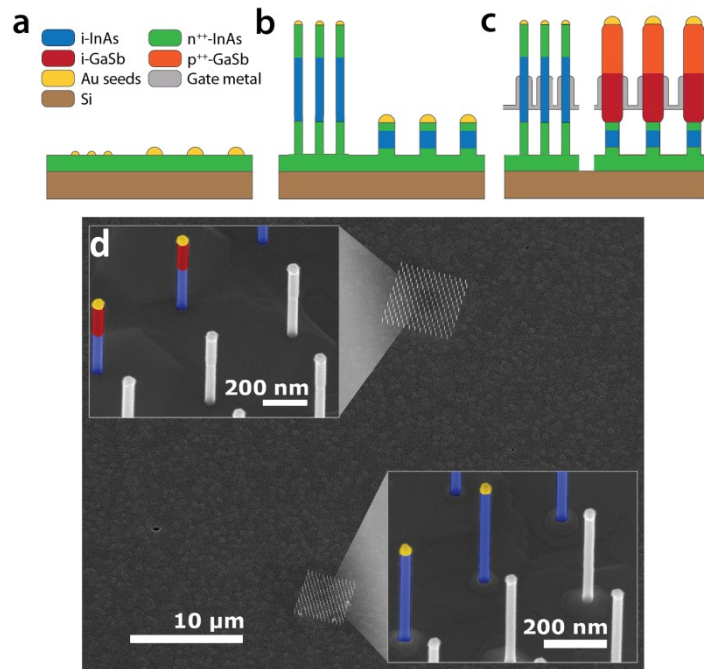


**Figure 1.** Schematic growth process and a SEM micrograph of a monolithic integration of InAs and GaSb nanowires on a Si substrate. (a) Au particles of different sizes are patterned by EBL on a Si substrate with a highly doped InAs layer. (b) InAs nanowire segments with an n-i-n doping profile are grown from the Au seed particles. The particle size and pitch is used to control the growth rate yielding both long thin wires and short wires with larger diameter simultaneously. (c) Growth continues with a GaSb segment with an i-p doping profile. The Gibbs-Thomson effect inhibits growth of GaSb on the thin InAs segments and careful tuning of the particle size and density is exploited to achieve similar total lengths of InAs and InAs/GaSb nanowires. The position of the gate for the n-InAs and p-GaSb MOSFETs and the InAs mesa isolation is indicated. (d) Partially colored SEM micrograph of InAs and InAs/GaSb nanowire arrays grown in a single MOCVD step.

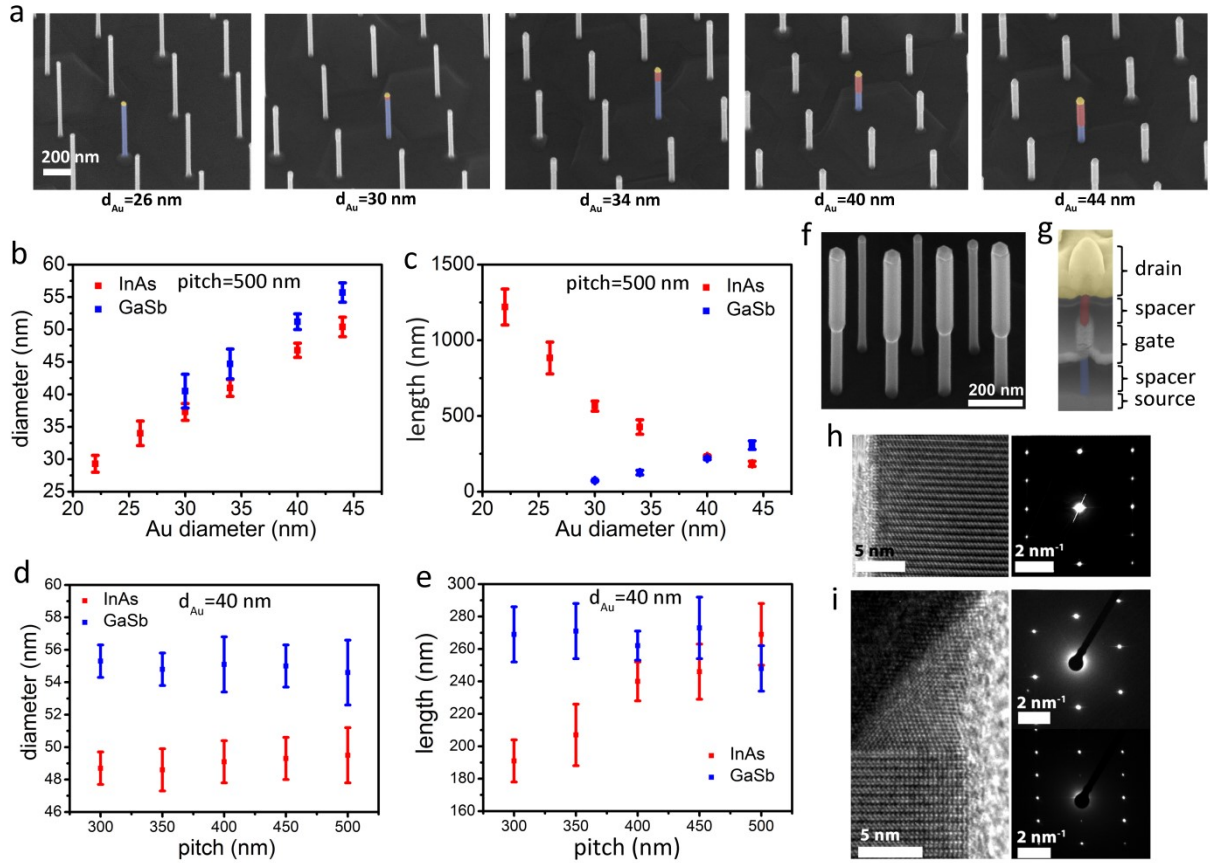


**Figure 2.** Control of nanowire dimensions. (a) Nanowires grown from Au particles with different diameter. The thinner and thicker nanowire segments have been attributed to InAs and GaSb respectively using XEDS analysis. The InAs segment is colored blue, the GaSb red and the Au particle yellow on single wires for clarity. For the smallest diameters the GaSb growth is completely suppressed. The GaSb segment length increases with increasing Au diameter while the InAs length decreases. (b) Diameter of the InAs and GaSb segments as a function of Au particle size. The mean diameter is calculated for 20 nanowires in each array and the error bars represent the standard deviation. An Au particle size  $d_{Au} > 30$  nm is necessary for the nucleation of GaSb. The diameters of both segments are correlated to the Au size. (c) Length of the InAs and GaSb segments as a function of Au particle size. The lengths of the InAs and GaSb segments decrease and increase with increasing  $d_{Au}$  respectively. This opposite trend of the axial growth rate can be attributed to the Gibbs-Thomson effect lowering the growth rate of GaSb for smaller Au particles. (d) Nanowire diameter as a function of pitch between Au particles. (e) Length of InAs and GaSb segments as a function of Au pitch. The

InAs and GaSb segments have all a diameter of 49 nm and 55 nm, respectively. The error bars in figures b to e represent the standard deviation. (f) InAs and InAs/GaSb nanowires with 200 nm pitch. (g) Partially colored cross sectional SEM image (52° tilt) of a finished MOSFET with an InAs/GaSb nanowire. (h) High resolution TEM image of an InAs nanowire with the corresponding diffraction pattern indicating a high quality wurtzite crystal structure. (i) TEM image of the heterojunction in an InAs/GaSb nanowire with the diffraction patterns from the top zincblende GaSb and the bottom wurtzite InAs segment. The crystal interface to the wurtzite InAs segment is sharp and the composition at the interface can be considered abrupt with only a 3.5 nm segment with intermediate composition as determined from an XEDS line scan (Supporting Information Figure S1).

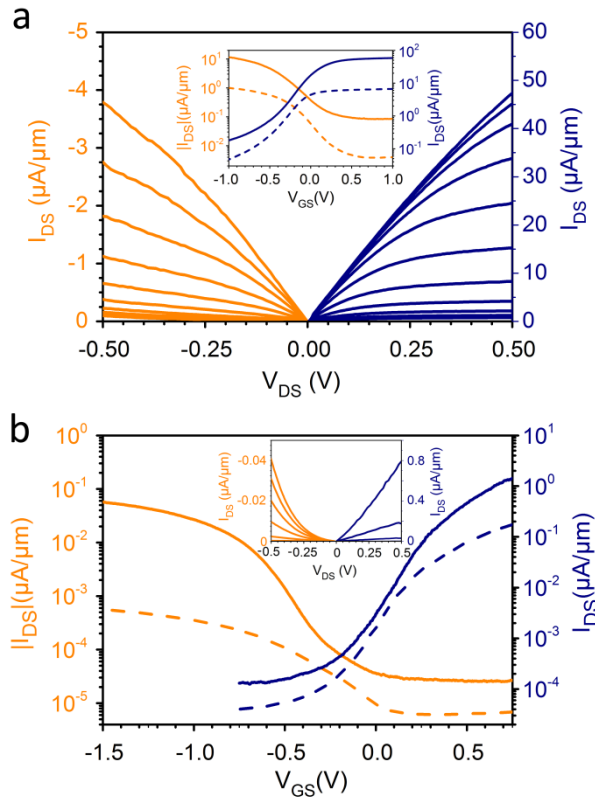


**Figure 3.** Output and transfer characteristics of InAs and GaSb MOSFETs. (a) Output and characteristics of an InAs MOSFET (blue) with a nanowire diameter  $d_{InAs} = 32$  nm and a GaSb MOSFET (orange) with  $d_{GaSb} = 48$  nm with  $-0.50 < V_{gs} < 0.5$  V (100 mV step). The inset displays the transfer characteristics with  $|V_{ds}| = 50$  mV (dashed) and  $|V_{ds}| = 500$  mV (solid). (b) Transfer characteristics of



MOSFETs where the thin GaSb shell has been removed with  $|V_{ds}| = 50$  mV (dashed) and  $|V_{ds}| = 500$  mV (solid). The InAs MOSFET (blue) has  $d_{\text{InAs}} = 34$  nm and the GaSb MOSFET (orange) has  $d_{\text{GaSb}} = 63$  nm. The inset displays the output characteristics with  $0 < V_{gs} < 0.75$  V (250 mV step) for InAs and  $-1.4$  V  $< V_{gs} < 0.2$  V (100 mV step) for GaSb.

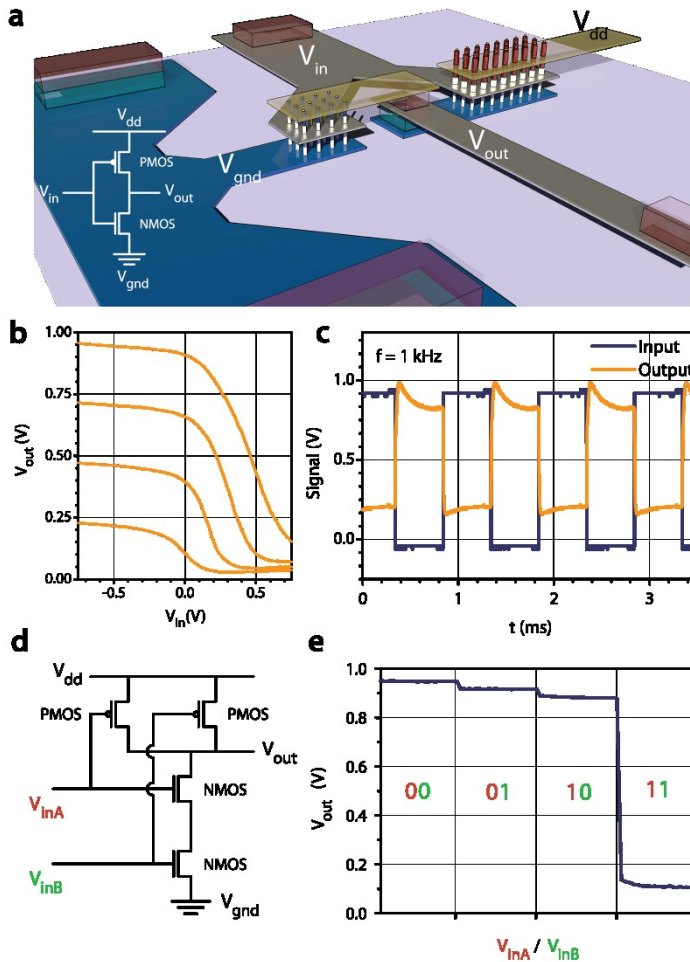


**Figure 4.** DC and AC inverter and NAND characteristics. (a) A schematic image of an inverter where the two spacer layers have been omitted for clarity. (b) Voltage transfer characteristics for an inverter with digitally etched nanowires for several supply voltages ( $V_{dd}$ ) ranging from 0.25 V to 1V (0.25 V steps). (c) AC characterization of an inverter circuit operating at 1 kHz with a 1 V square-wave input signal. (d) NAND circuit schematic and (e) NAND characteristic with a power supply voltage of  $V_{dd} = 1$  V and input voltages of  $V_{inA} / V_{inB} = \pm 1$  V.